

Simplex valence-bond crystal in the spin-1 kagome Heisenberg antiferromagnet

Tao Liu¹, Wei Li², Andreas Weichselbaum², Jan von Delft², and Gang Su^{1*}

¹*Theoretical Condensed Matter Physics and Computational Materials Physics Laboratory, School of Physics, University of Chinese Academy of Science, Beijing 100049, China*

²*Physics Department, Arnold Sommerfeld Center for Theoretical Physics, and Center for NanoScience, Ludwig-Maximilians-Universität, 80333 Munich, Germany*

(Dated: December 3, 2024)

We investigate the ground state properties of a spin-1 kagome antiferromagnetic Heisenberg (KAH) model using tensor-network methods. We find a trimerized ground state, with energy per site $e_0 \approx -1.409$ obtained by accurate calculations directly in the thermodynamic limit. The symmetry between left and right triangles is spontaneously broken, with a relative energy difference of $\delta \approx 20\%$. The spin-spin, dimer-dimer, and chiral correlation functions are found to decay exponentially with a rather short correlation length, showing that the ground state is gapped. Based on this unambiguous numerical evidence, we identify the ground state of the spin-1 KAH model to be a simplex valence-bond crystal (SVBC). Besides the KAH model, we also discuss the spin-1 bilinear-biquadratic Heisenberg model on a kagome lattice, and determine its ground state phase diagram. In particular, we find a quantum phase transition between the SVBC and ferro-quadrupolar nematic states.

PACS numbers: 75.10.Jm, 75.10.Kt, 05.10.Cc

Introduction.— Geometrical frustration, as a particularly interesting phenomenon in quantum antiferromagnets, has raised enormous interest recently [1]. It arises when any classical (Ising) spin configuration cannot satisfy simultaneously all the local terms in the Hamiltonian, which leads to a macroscopic degeneracy and thus greatly enhances quantum fluctuations. Frustration might melt semiclassical spin orders (including magnetic or valence bond order, etc.), driving the system into an exotic quantum state called quantum spin liquid [2, 3]. Some typical frustrated antiferromagnets include the spin-1/2 and spin-1 Heisenberg models on the triangular lattice [4, 5], spin-1/2 J_1 - J_2 square [6–8], and the pyrochlore [9] lattices. Among others, the spin-1/2 kagome antiferromagnetic Heisenberg (KAH) model is one of the most intriguing frustrated models: its ground state is widely believed to be a spin liquid [10–14], but its nature is still under debate [15].

KAH models with higher spins are less well-studied, despite their physical realizations in experiments [16, 17], where the synthesized materials have spin-spin couplings which can be effectively described by a Heisenberg model. The ground state properties of the relevant spin-1 KAH are still far from clear. Interesting variational wavefunctions have been proposed (for instance, the static or resonating loop states [18–20], or the hexagon solid state [21]), yielding some preliminary advances towards understanding the nature of the ground state. Notably, Cai *et al.* considered a completely trimerized variational wavefunction on the kagome lattice [20], with all the spin-1's in each left (or right) triangle forming a SU(3) singlet (trimerization). However, the corresponding variational energy of this simple valence-bond crystal is $e_0 = -1$ per site, much higher than that of the resonating Affleck-Kennedy-Lieb-Tasaki loop (RAL) state ($e_0 \approx -1.27$) which retains the vertex-centered inversion symmetry. The RAL state has been shown to be a \mathbb{Z}_2 spin liquid with symmetry fractionalization [19]. The nature of the true ground state of the spin-1 KAH model is still an open question.

In this work, we employ state-of-the-art tensor network al-

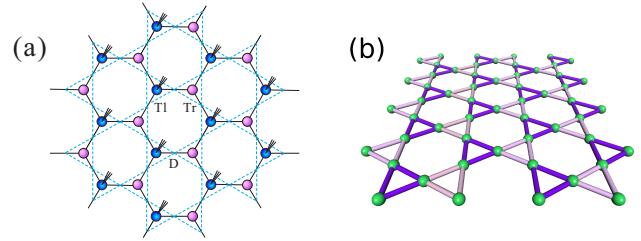


FIG. 1. (Color online) (a) Kagome lattice (dotted lines) and the initial setup of the tensor-network wavefunction (solid lines). T_l and T_r are the triangle tensors and D is the bond dimension. (b) Illustration of the simplex valence-bond crystal. The two kinds of triangles or “simplexes” (marked light and dark purple) have different energies, and a lattice inversion symmetry is spontaneously broken.

gorithms to study the properties of spin-1 KAH model. We use imaginary-time evolution and adopt the Bethe-lattice approximation (i.e., the simple update scheme) for truncation [22–24] to obtain a tensor-network variational ground state wavefunction. We then insert the resulting tensors into an infinitely large two-dimensional (2D) lattice [Fig. 1 (a)], and determine the variational ground state energy as $e_0 \approx -1.409$. Lattice inversion (reflection) symmetry is found to be broken, where the two kinds of triangles (or simplexes) have different energy expectation values [See Fig. 1 (b)]. We thus call the ground state a simplex valence-bond crystal (SVBC). We also roll up the tensor networks on cylinders with various circumferences, and evaluate their variational energies, as well as the entanglement entropies, through exact contractions. The entanglement entropy shows that the ground state of the spin-1 KAH model may have a nontrivial topology. Aside from the KAH, we also consider the spin-1 bilinear-biquadratic (BLBQ) Heisenberg model on the kagome lattice, and obtain its ground state phase diagram. We find the SVBC state to be the ground state throughout an extended regime in the phase diagram, and observe a quantum phase transition

between the SVBC and ferro-quadrupolar states is observed at $\theta_c \approx -0.04\pi$.

Model and Method.— We consider the quantum spin-1 KAH model with only nearest-neighbor isotropic exchange interactions, whose Hamiltonian is $H = \sum_{\langle i,j \rangle} \mathbf{S}_i \cdot \mathbf{S}_j$, with spin operator \mathbf{S}_i on sites i , while $\langle i,j \rangle$ stands for the nearest-neighbor link on a lattice. We use the projected entangled-pair state (PEPS) as a wavefunction ansatz [25], and invoke an imaginary-time evolution to seek the best variational ground state. Choosing a random state $|\psi_0\rangle$ as the starting point, we get the “true” ground state in the “long-time” limit using $|\psi_g\rangle = \lim_{\beta \rightarrow \infty} e^{-\beta H} |\psi_0\rangle$. In practice, we take the first order Trotter-Suzuki decomposition [26] to approximate $e^{-\beta H}$ by the product of a series of evolution gates $e^{-\beta H} = (e^{-\tau H})^K$, with $K\tau = \beta$. For small τ , it can be further decomposed as $e^{-\tau H} \approx \prod_{\triangleright, \triangleleft} e^{-\tau h_\triangleright} e^{-\tau h_\triangleleft}$, with h_α the three-site local Hamiltonian in a single triangle, $\alpha \in \{\triangleright, \triangleleft\}$. $e^{-\tau h_\alpha}$ can be applied to the wavefunction successively.

The initial tensor network [Fig. 1(a)] is set up as a honeycomb lattice, with two kinds of tensors, T_l and T_r , associated with all left and all right triangles of the lattice, respectively. T_l (blue circle) has three physical and three geometric indices. T_r (red circle) only has three geometric indices. Such a tensor network ansatz is also called projected entangled simplex state [27]. After absorbing a three-site projection operator $e^{-\tau H_\triangleright}$ with the tensor T_l , we make a decomposition

$$(T_l)_{\tilde{x}, \tilde{y}, \tilde{z}}^{p_1, p_2, p_3} = \sum_{x, y, z} (\tilde{T}_l)_{x, y, z} (U_x)_{x, \tilde{x}}^{p_1} (U_y)_{y, \tilde{y}}^{p_2} (U_z)_{z, \tilde{z}}^{p_3}, \quad (1)$$

where $U_{x, y, z}$ can be obtained by higher-order singular value decomposition. Then, T_l is replaced by a tensor \tilde{T}_l without physical indices. Subsequently, we associate the three U tensors with T_r , and update it with \tilde{T}_r using

$$(\tilde{T}_r)_{\tilde{x}, \tilde{y}, \tilde{z}}^{p_1, p_2, p_3} = \sum_{x, y, z} (T_r)_{x, y, z} (U_x)_{x, \tilde{x}}^{p_1} (U_y)_{y, \tilde{y}}^{p_2} (U_z)_{z, \tilde{z}}^{p_3}. \quad (2)$$

After this tensor-network transformation, the three physical indices have moved from T_l to \tilde{T}_r and we can proceed to act with the projection $e^{-\tau H_\triangleleft}$ on \tilde{T}_r . This procedure can be repeated until the tensors T_l and T_r reach “fixed” points. Note that the geometric bond dimensions D of the tensors would grow after each projection step. To make our calculation sustainable, we truncate the state space by taking the transformations $U_{x, y, z}$ to be isometries instead of unitary matrices. Here we use a Bethe-lattice approximation for truncation [22, 23], following Refs. 24 and 28.

In our simulations, we set $\tau = 0.1$ at the beginning, and gradually reduce it to 10^{-5} . The energy expectation values decrease with the imaginary-time evolution steps, and we stop when the energies have converged within a prescribed accuracy of, say, 10^{-10} .

To calculate observables $\langle O \rangle = \frac{\langle \Psi | O | \Psi \rangle}{\langle \Psi | \Psi \rangle}$, we need to contract the shared physical indices between tensor network $|\Psi\rangle$ and its conjugate $\langle \Psi|$, and hence arrive at a 2D double-layer tensor network. In the following, we mainly consider two kinds

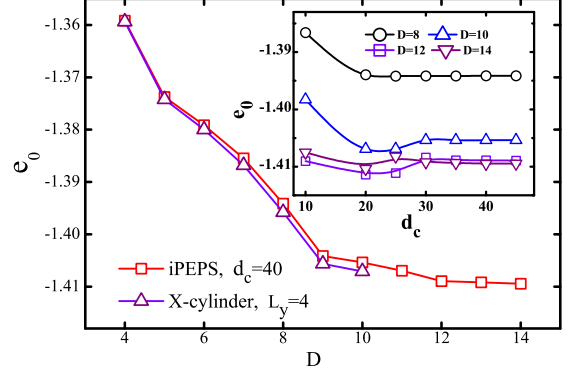


FIG. 2. (Color online) The variational ground state energy per site e_0 . The squares are iPEPS data from infinite 2D lattice calculations, while the triangles are calculated on XC8 cylinders with perimeter $L_y = 4$. e_0 decreases with increasing D and converges well for $D \geq 12$, towards $e_0 \approx -1.409$. The inset shows the energy convergence with d_c for various bond dimensions D .

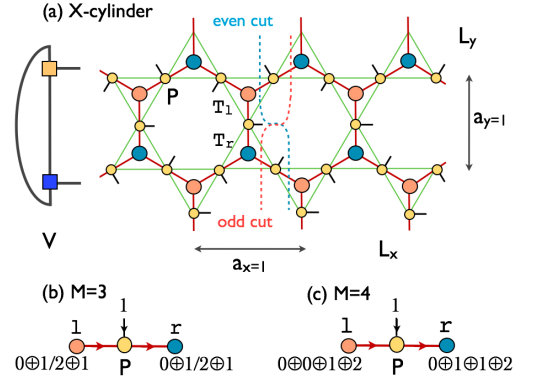


FIG. 3. (Color online) (a) Illustration of the X-cylinder. L_x is the length along the horizontal direction (open boundary condition, with length unit a_x), L_y is the circumference of the cylinder (periodic boundary condition, with length unit a_y). Starting contractions from the open end, one gets the boundary vector V , which represents the contracted part of tensor network on the cylinder. Depending on whether the three physical indices are associated with T_l or T_r , one can cut the cylinder in two differently ways, called odd or even cut. (b,c) Implementation of $SU(2)$ symmetry in local tensors, M labels the number of multiplets included. The spin quantum numbers of acillas are also shown, and the arrows indicate how the spin multiplets are fused together [29].

of geometries: (a) an infinitely large 2D lattice and (b) an infinitely long cylinder with finite circumference. For case (a), we adopt the infinite PEPS (iPEPS) technique [30–32] to contract the tensor network. During the contractions, the geometric bond of the boundary matrix product state (MPS) is truncated to at most d_c bond states. For tensors with different geometric bond dimensions D , we need different truncation dimensions d_c . As can be seen in Fig. 2, the calculated ground energies are well converged when $d_c \geq 35$ for $D = 8 \sim 14$.

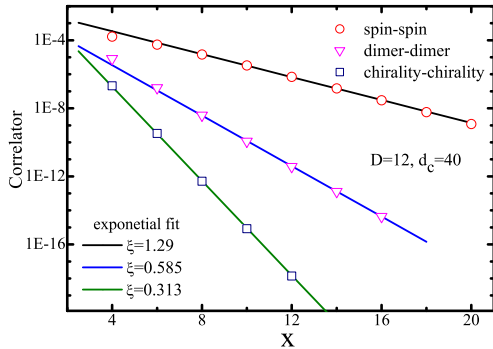


FIG. 4. (Color online) Spatial dependence of spin-spin, dimer-dimer, and chiral correlation functions (symbols) on a log-linear scale, together with exponential fits (solid lines) that yield the correlation length ξ . The correlation functions are calculated by iPEPS on an infinite kagome lattice. x is the distance between triangles with length unit a_x .

Ground state energy and valence-bond crystal.— Fig. 2 presents our results of energy per site e_0 . The inset shows that the energy results are well converged for boundary MPS bond dimension $d_c = 40$. The main panel, where $d_c = 40$, shows that the energy decreases monotonically with increasing bond dimension D , converging for $D \geq 12$. The value $e_0 \approx -1.409$ obtained for $D = 14$ constitutes our best estimate of the ground state energy in the thermodynamic limit.

In addition, we also wrap the tensor networks on the $L_y = 4$ cylinder and perform the contraction exactly. We adopt the X-cylinder geometry shown in Fig. 3 (a) (and denoted XC8 in previous work on kagome cylinder [10, 11]). We start from both ends, contract the boundary vector [V in Fig. 3 (a)] with a column of tensors, and repeat this process until convergence is reached. The cylinder results for e_0 are also presented in Fig. 2, they are slightly lower than the iPEPS data, owing to the finite circumference. In contrast to the approximate iPEPS contraction, the exact contraction is fully controlled and yields a true variational upper bound e_0 on a given cylinder.

In Fig. 4, we show the spin-spin, dimer-dimer, and chiral correlation functions, all evaluated between two triangles belonging to the same kind, say, left-handed triangles. The dimer-dimer correlation function is defined by $\langle D_i D_j \rangle = \langle (S_i^z S_{i+1}^z) \cdot (S_j^z S_{j+1}^z) \rangle - \langle S_i^z S_{i+1}^z \rangle \cdot \langle S_j^z S_{j+1}^z \rangle$, where i and j belong to different triangles. The chiral correlation function is defined as $\langle C_m C_n \rangle = \langle [\mathbf{S}_{m_1} \cdot (\mathbf{S}_{m_2} \times \mathbf{S}_{m_3})][\mathbf{S}_{n_1} \cdot (\mathbf{S}_{n_2} \times \mathbf{S}_{n_3})] \rangle$, where m, n label positions of two triangles, and m_i, n_i label the positions of the three sites within a triangle. Fig. 4 shows that all these correlation functions decay exponentially, implying that the ground state of spin-1 KAH model is gapped and there is no magnetic order.

Fig. 5 shows the energy difference $\Delta E = \frac{2}{3}|E_l - E_r|$ between left- and right-handed triangles, as a function of D . For $D \geq 12$ it converges to $\Delta E \approx 0.283$ (with a relative difference $\delta = \Delta E/e_0 \approx 20\%$). The fact that ΔE is nonzero implies that the ground state spontaneously breaks lattice inversion

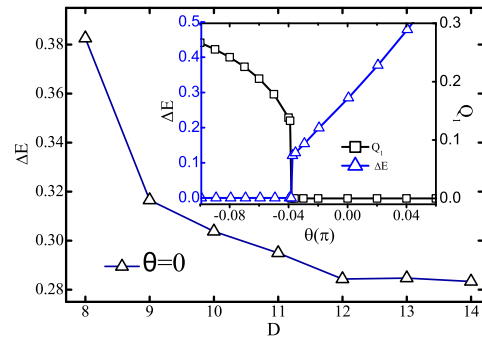


FIG. 5. (Color online) Energy difference $\Delta E = 2(E_l - E_r)/3$, between left- and right-handed triangles, evaluated at Heisenberg point ($\theta = 0$) on an infinite lattice with iPEPS, and plotted as function of D , showing convergence for $D \geq 12$. The inset shows that ΔE vanishes when $\theta < -0.04\pi$, where ferromagnetic quadrupolar order (Q_1) sets in.

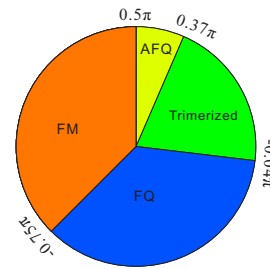


FIG. 6. (Color online) Ground state phase diagram of the spin-1 bilinear-biquadratic Heisenberg model on the Kagome lattice.

symmetry. Note, although our method is initially biased in its treatment of left- and right-triangles, by the end of the projections we reduce τ to 10^{-5} , restoring the equivalence between the two kinds of triangles. Therefore, we believe that the observed spontaneous trimerization is not a artifact. In fact, we do not find any symmetry breaking when using small bond dimensions (say, $D \leq 7$); the trimerization sets in only when we increase the bond dimension and get a variational energy close to the “true” ground state value.

Bilinear-biquadratic Heisenberg model.— We also studied the spin-1 BLBQ Heisenberg model with Hamiltonian

$$H = \sum_{\langle i,j \rangle} [\cos \theta (\mathbf{S}_i \cdot \mathbf{S}_j) + \sin \theta (\mathbf{S}_i \cdot \mathbf{S}_j)^2], \quad (3)$$

which recovers the KAH model when $\theta = 0$. When we tune θ away from the Heisenberg point, we see that the SVBC state belongs to an extended phase. The results are shown in the inset of Fig. 5. The energy differences are verified to be robust for various θ 's. Interestingly, when we tune θ to the negative side, a phase transition occurs at the transition point $\theta_c \approx -0.04$, where the trimerization vanishes, and the system turns into a non-magnetic phase which has ferro-quadrupolar (FQ) order, $Q_1 = \langle S_x^2 - S_y^2 \rangle \neq 0$.

In Fig. 6 shows the ground state phase diagram of the spin-1 kagome BLBQ Heisenberg model obtained by exploring

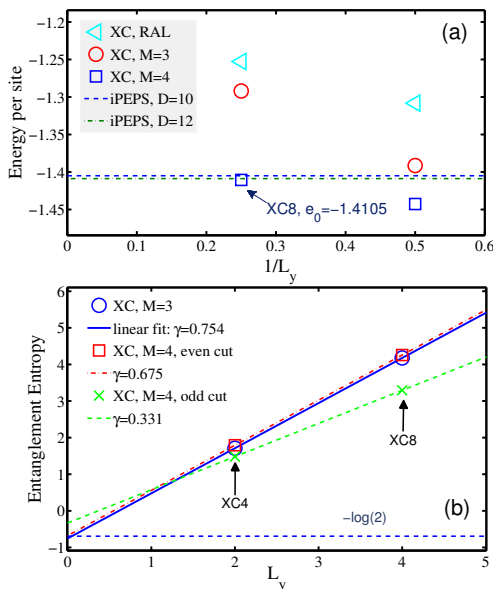


FIG. 7. (Color online) (a) Energy per site and (b) von Neumann entanglement entropies of the tensor-network variational wavefunctions on cylinders. For $L_y = 2$ or 4 , we used the XC4 or XC8 cylinder, respectively.

other θ values. There are four phases in total: a FQ phase ($-3/4\pi < \theta < -0.04\pi$), a SVBC phase ($-0.04\pi < \theta < 0.37\pi$), an antiferro-quadrupolar (AFQ) phase ($0.37\pi < \theta < 1/2\pi$), $\mathbf{Q}_{tot} = \sum_{i \in \Delta} \mathbf{Q}_i = \mathbf{0}$, but $\mathbf{Q}_i \neq \mathbf{0}$), and a ferromagnetic (FM) phase ($1/2\pi < \theta < 5/4\pi$). Note that the SU(3) point ($\theta = \pi/4$) lies in the SVBC phase, thus the SU(3) Heisenberg model also has a trimerized ground state. This observation is in agreement with a previous study of the SU(3) model [33].

SU(2) PEPS algorithm.— Since we perform the contraction of the cylinder tensor network exactly, the computational costs grow exponentially with circumference L_y . To reduce these costs, we have implemented non-abelian SU(2) symmetry in the local tensors, which facilitates both the imaginary time projection and exact contraction processes, improving the efficiency and robustness of the algorithms. To this end, we employed the “QSpace” tensor library, which implements non-abelian symmetries in tensor networks in a transparent framework [34]. We considered two cases, namely $M = 3$ and $M = 4$, where M labels number of retained multiplets on the geometric bonds [see Fig. 3 (b,c)]. The $M = 3$ state contains the spin multiplets $0 \oplus 1/2 \oplus 1$ in the geometric bond (equivalent to $D = 6$ plain tensors used before), and $M = 4$ means $0 \oplus 0 \oplus 1 \oplus 2$ ($D = 10$) or $0 \oplus 1 \oplus 1 \oplus 2$ ($D = 12$). These specific multiplets automatically appear in the simple-update optimization procedure, where we only specify the number M of retained multiplets.

Fig. 7 (a) shows the energy expectation values of $M = 3, 4$ tensor networks on X-cylinders with circumferences $L_y = 2, 4$ (XC4 and XC8, respectively). The $M = 3$ state already has a somewhat lower energy than the RAL state, while $M = 4$ yields a further gain in energy with $e_0 = -1.4105$ for $L_y = 4$

(XC8). In addition, trimerization can also be clearly identified in the optimized $M = 4$ state, again with a relative difference 20%, in agreement with our plain tensor-network (iPEPS) calculations which do not exploit symmetries.

Topological entanglement entropy.— To study topological properties, we wrap the tensor network on an infinitely long X-cylinder (with finite circumference), and cut it into two halves. Following the PEPS technique developed in Ref. 35, we evaluate the von Neumann entropy, $S = -\text{Tr}[\rho \log(\rho)]$. For gapped ground states of short-ranged Hamiltonians in 2D, the entanglement entropy scales as $S \simeq cL_y - \gamma$ on the cylinder, with L_y the cylinder perimeter. The leading term reflects the entanglement area law, and the subleading term γ is a constant which is nonzero when the state possesses nontrivial topology [12]. $\gamma (\neq 0)$ is thus called the topological entanglement entropy (TEE) [36, 37].

Fig. 7(b) shows the von Neumann entropies of $M = 3, 4$ states on X-cylinders with $L_y = 2, 4$. For the $M = 3$ state, S extrapolates to $\gamma = 0.76 \approx \log(2)$. Note that both the RAL state [19] and the $M = 3$ state obtained by imaginary time projection have virtual spins $0 \oplus 1/2 \oplus 1$. Since the $M = 3$ state here has a similar energy and TEE [namely $\log(2)$] as the RAL state, and since neither of them have magnetic or valence-bond ordering, we expect that, just as the RAL state, the optimized $M = 3$ state is a \mathbb{Z}_2 spin liquid, too.

Although retaining $M = 4$ multiplets clearly lowers the energy relative to $M = 3$, it hardly alters the entanglement entropy, which also extrapolates to a nonzero value for $-\gamma$ [Fig. 7(b)]. In addition, there is a subtlety in the $M = 4$ state, which does not appear in the $M = 3$ case, when we cut the cylinder into two halves. As shown in Fig. 3(b,c), after the optimization, the two indices of the tensor P are found to have different multiplet structures, $0 \oplus 0 \oplus 1 \oplus 2$ or $0 \oplus 1 \oplus 1 \oplus 2$, for the left or right geometric bond, respectively. Because of this inequivalence between the two geometric bonds (and also because of the spontaneous trimerization), the cylinder can be cut in two inequivalent ways, called even or odd cut [see Fig. 3(a)], depending on how we associate physical indices with the triangle tensors. This leads to even and odd entanglement entropies as shown in Fig. 7(b). The even entanglement entropy extrapolates to $\gamma = 0.67 \approx \log(2)$, while the odd one yields $\gamma = 0.331$, which deviates from $\log(2)$. We ascribe this deviation to a finite-circumference effect. The next-larger XC12 cylinder has circumference $L_y = 6$, which is beyond our computational capacity at present, so we leave this issue for a future study.

Conclusion.— We find the ground state of the spin-1 KAH model to be a gapped trimerized state (simplex valence-bond crystal). Its entanglement properties suggest that it possesses nontrivial topological order; exploring the latter in more detail poses an interesting challenge for future studies. An important technical innovation of our work is the explicit implementation of SU(2) symmetry in our PEPS-based algorithms; this not only enhances their numerical performance, but has also enabled us to explicitly specify the bond multiplets to be used, thus establishing a link between our optimized states and the

topological RAL state.

Acknowledgement.— WL was indebted to Hong-Hao Tu, Meng Cheng, Shuo Yang, and Zi Cai for stimulating discussions. TL thanks Guang-Zhao Qin for his help in the schematic plot Fig. 1(b). We acknowledge Hong-Chen Jiang and Shou-Shu Gong for discussions about the DMRG calculations of the same model. This work was supported in part by the MOST of China (Grant No. 2012CB932900 and No. 2013CB933401), and the Strategic Priority Research Program of the Chinese Academy of Sciences (Grant No. XDB07010100). WL was also supported by the DFG through SFB-TR12 and NIM. WL acknowledges the hospitality of the Max-Planck Institute for Quantum Optics, where part of the work has been performed.

Note added.— Upon finalizing the manuscript we noticed a recent preprint on density matrix renormalization group study of spin-1 kagome Heisenberg model with similar conclusions [38].

* gsu@ucas.ac.cn

- [1] G. Misguich and C. Lhuillier, *Frustrated Spin Systems*, edited by H. T. Diep (World Scientific, Singapore, 2005).
- [2] P. A. Lee, *Science* **321**, 1306 (2008).
- [3] L. Balents, *Nature* **464**, 199 (2010).
- [4] Steven R. White and A. L. Chernyshev, *Phys. Rev. Lett.* **99**, 127004 (2009).
- [5] A. Läuchli, F. Mila, and K. Penc, *Phys. Rev. Lett.* **97**, 087205 (2006).
- [6] H.-C. Jiang, H. Yao, and L. Balents, *Phys. Rev. B* **86**, 024424 (2012).
- [7] S.-S. Gong, W. Zhu, D.-N. Sheng, O. I. Motrunich, and M. P. A. Fisher, [arXiv:1311.5962](https://arxiv.org/abs/1311.5962) (2013).
- [8] L. Wang, Z.-C. Gu, F. Verstraete, X.-G. Wen, [arXiv:1112.3331](https://arxiv.org/abs/1112.3331) (2011); L. Wang, D. Poilblanc, Z.-C. Gu, X.-G. Wen, F. Verstraete, *Phys. Rev. Lett.* **111**, 037202 (2013).
- [9] S. T. Bramwell, M. J. P. Gingras, *Science* **294**, 1495 (2001).
- [10] S. Yan, D. A. Huse, and S. White, *Science* **332**, 1173 (2011).
- [11] S. Depenbrock, I. P. McCulloch, and U. Schollwöck, *Phys. Rev. Lett.* **109**, 067201 (2012).
- [12] H.-C. Jiang, Z. Wang, and L. Balents, *Nature Phys.* **8**, 902 (2012).
- [13] D. Poilblanc, N. Schuch, D. Perez-Garcia, J. I. Cirac, *Phys. Rev. B* **86**, 014404 (2012); D. Poilblanc, N. Schuch, *Phys. Rev. B* **87**, 140407 (2013).
- [14] S.-S. Gong, W. Zhu, and D. N. Sheng [arXiv: 1312.4519](https://arxiv.org/abs/1312.4519) (2013).
- [15] Y. Iqbal, F. Becca, S. Sorella, and D. Poilblanc, *Phys. Rev. B* **87**, 060405 (2013).
- [16] N. Wada, T. Kobayashi, H. Yano, T. Okuno, A. Yamaguchi, K. Awaga, *J. Phys. Soc. Jpn.* **66**, 961 (1997).
- [17] G. Lawes, M. Kenzelmann, N. Rogado, K. H. Kim, G. A. Jorge, R. J. Cava, A. Aharony, O. Entin-Wohlman, A. B. Harris, T. Yildirim, Q. Z. Huang, S. Park, C. Broholm, and A. P. Ramirez, *Phys. Rev. Lett.* **93**, 247201 (2004).
- [18] H. Yao, L. Fu, and X.-L. Qi, [arXiv:1012.4470](https://arxiv.org/abs/1012.4470) (2010).
- [19] W. Li, S. Yang, M. Cheng, Z.-X. Liu, and H.-H. Tu, *Phys. Rev. B* **89**, 174411 (2014).
- [20] Z. Cai, S. Chen, and Y. P. Wang, *J. Phys.: Condens. Matter*, **21**, 456009 (2009); Z. Cai, S. Chen, S. P. Kou, and Y. P. Wang, *Phys. Rev. B* **76**, 054443 (2007).
- [21] K. Hida, *J. Phys. Soc. Jpn.* **70**, 3673 (2001); *J. Phys. Soc. Jpn.* **71**, 3021 (2002).
- [22] H.-C. Jiang, Z.-Y. Weng, T. Xiang, *Phys. Rev. Lett.* **101**, 090603 (2008).
- [23] W. Li, J. von Delft, and T. Xiang, *Phys. Rev. B* **86**, 195137 (2012).
- [24] T. Liu, S.-J. Ran, W. Li, X. Yan, Y. Zhao and G. Su, *Phys. Rev. B* **89**, 054426 (2014).
- [25] F. Verstraete and J. I. Cirac, [arxiv:cond-mat/0407066](https://arxiv.org/abs/cond-mat/0407066); F. Verstraete and J. I. Cirac, *Phys. Rev. A* **70**, 060302 (2004).
- [26] M. Suzuki and M. Inoue, *Prog. Theor. Phys.* **78**, 787 (1987); M. Inoue and M. Suzuki, *Prog. Theor. Phys.* **79**, 645 (1988).
- [27] Z.-Y. Xie, J. Chen, J.-F. Yu, X. Kong, B. Normand, T. Xiang, *Phys. Rev. X* **4**, 011025 (2014).
- [28] S.-J. Ran, W. Li, B. Xi, Z. Zhang and G. Su, *Phys. Rev. B* **86**, 134429 (2012).
- [29] Using the PEPS construction, geometric bonds are associated with auxiliary orthonormal state spaces that can be categorized according to the symmetries of the system. Through tensors, these state spaces are fused with others, as indicated by the arrows with all lines. Since the direction of arrows can be changed throughout the algorithm, there are no arrows shown with the lines in panel (a). Details will be published elsewhere.
- [30] J. Jordan, R. Orus, G. Vidal, F. Verstraete, and J. I. Cirac, *Phys. Rev. Lett.* **101**, 250602 (2008).
- [31] R. Orus and G. Vidal, *Phys. Rev. B* **80**, 094403 (2009); R. Orus, *Phys. Rev. B* **85**, 205117 (2012).
- [32] R. Orus and G. Vidal, *Phys. Rev. B* **78**, 155117 (2008).
- [33] P. Corboz, K. Penc, F. Mila, and A. M. Läuchli, *Phys. Rev. B* **86**, 041106(R).
- [34] A. Weichselbaum, *Ann. Phys.* **327**, 2972 (2012).
- [35] J. I. Cirac, D. Poilblanc, N. Schuch, and F. Verstraete, *Phys. Rev. B* **83**, 245134 (2011).
- [36] A. Kitaev and J. Preskill, *Phys. Rev. Lett.* **96**, 110404 (2006).
- [37] M. Levin and X.-G. Wen, *Phys. Rev. Lett.* **96**, 110405 (2006).
- [38] H. J. Changlani and A. M. Läuchli, [arXiv:1406.4767](https://arxiv.org/abs/1406.4767) (2014).

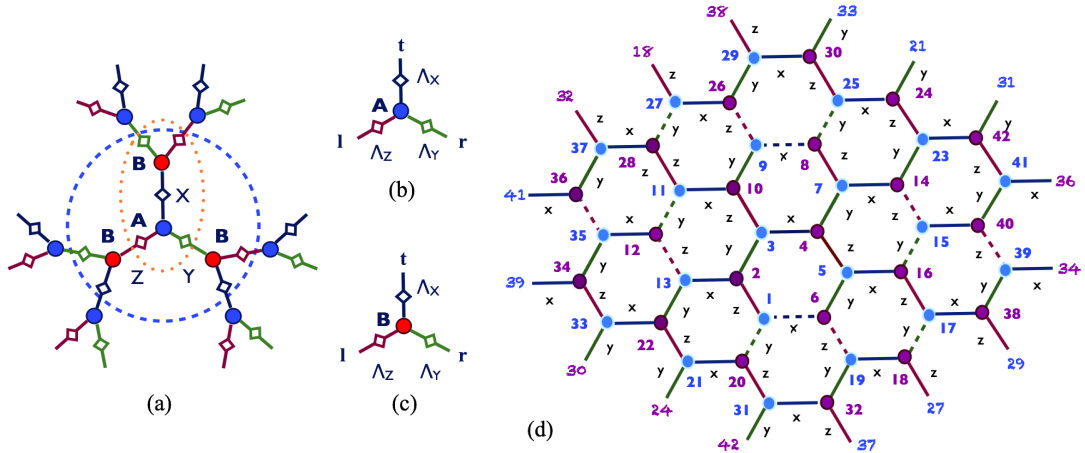


FIG. S1. (Color online) (a) The cluster in Bethe approximation of honeycomb lattice. (b,c) Local tensors determined by simple update. (d) Generalization of Bethe-lattice approximation to larger cluster with 42 sites.

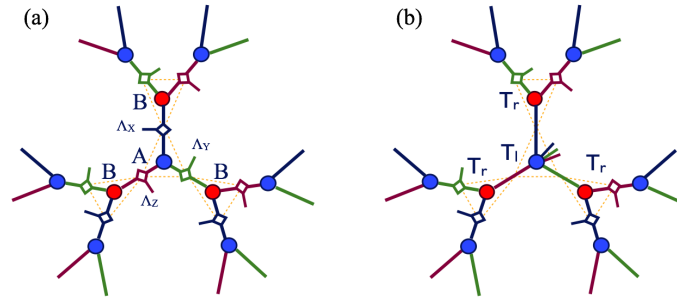


FIG. S2. (Color online) (a) The cluster in “Bethe-lattice approximation” of kagome lattice, which consists of three triangles, A, B are triangle tensors and $\Lambda_{x,y,z}$ (with physical indices) are located on the geometric bonds. (b) Associate three physical indices with one triangle tensor T_l , we get the tensors used in practical calculations.

Bethe-lattice Approximation (Simple update)

In this part we describe the method employed to optimize the tensors, the simple update, and its interpretation as a Bethe-lattice approximation. We start from the honeycomb lattice, whose minimal cluster problem (in Beth-lattice approximation) is shown in Fig. S1(a). We treat the couplings between the four sites within the dashed blue circle exactly, and update the subsystem (during the imaginary time evolution) with the help of environments. To be specific, the entanglement between the cluster and the rest are well approximated by the objects $\Lambda_{x,y,z}$ on the geometric bonds which play an important role in the bond truncations. The Λ 's are determined iteratively and self-consistently during the imaginary time evolution.

This method, dubbed as simple update [22], recovers the iTEBD method in one dimension (1D) [32], a quasi-optimal way to truncate the geometric bonds and update the tensors in 1D. In higher spatial dimensions, this method is quasi-optimal only on the Bethe lattice (thus it is called the Bethe-lattice approximation) [23], where the spatial dimension goes to infinite; while for intermediate dimensions, say 2D, unfortunately, this method is only an approximation.

Bethe-lattice approximation is scalable. Knowing the fact that the simple update is actually solving a cluster problem with special boundary, one can follow the idea developed in statistical mechanics and generalize the simple update to larger clusters [see Fig. S1 (d) for an example of 42-site cluster]. The clusters connect each other and form a super Bethe lattice, with which the Bethe-lattice approximations can be improved [23].

On the other hand, for the kagome lattice, the (minimal) cluster contains nine sites in total, and the corresponding infinite-dimensional lattice (where the simple update works quasi-optimally) is consisted of corner-sharing triangles (see dashed triangles in Fig. S2). This dual geometry of the Bethe lattice is called the Husimi lattice. Associating each triangle a tensor, we can obtain again a Bethe-lattice tensor network, and reuse the techniques developed in honeycomb lattice [24]. Note that now the Λ 's have additional physical indices, and the (triangle) projection operator contains three instead of two sites (bond projector) in

honeycomb case [Fig. S2 (a)].

In practice, we do not store Λ 's explicitly, but rather associate them with A (B) and obtain the triangle tensors T_l (T_r) [Fig. S2(b)]. Obtaining the local tensors (by solving the local cluster problem), we can rewire the tensors on an infinite 2D lattice or on a cylinder, and evaluate the observables with accurate PEPS techniques.